Supporting information for:

Unveiling mechanistic implications of water oxidation reaction boosted by guanidine proton relay: a chemical-electrochemical-chemical pathway and a non-concerted proton-electron transfer

Mojtaba Shamsipur*, Moslem Ardeshiri, Avat (Arman) Taherpour, Afshin Pashabadi*

Department of Chemistry, Razi University, Kermanshah, Iran

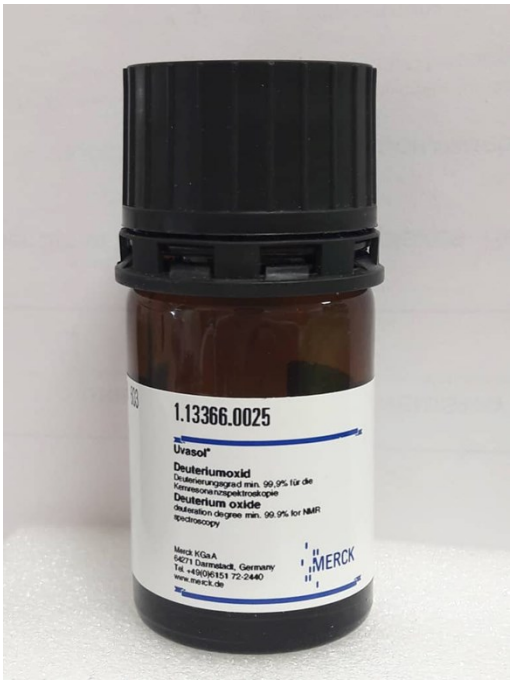

Figure S1. Image taken from the deuterimoxide 99.9% used in the isotopic studies.

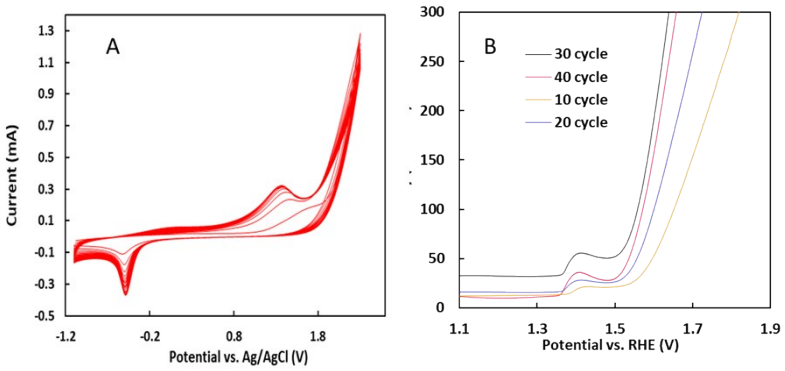

Figure S2. (A) Cyclic voltammograms for the electrochemical polymerization of 2.5 mM arginine on NF at the scan rate of 100 mV/s. (B) Effect cycle-number during electropolymerization of Arg (at NF/$NiCo_2O_4$/MnP) on OER activity in 0.5 M of KOH with scan rate of 5 mV s^{-1}.

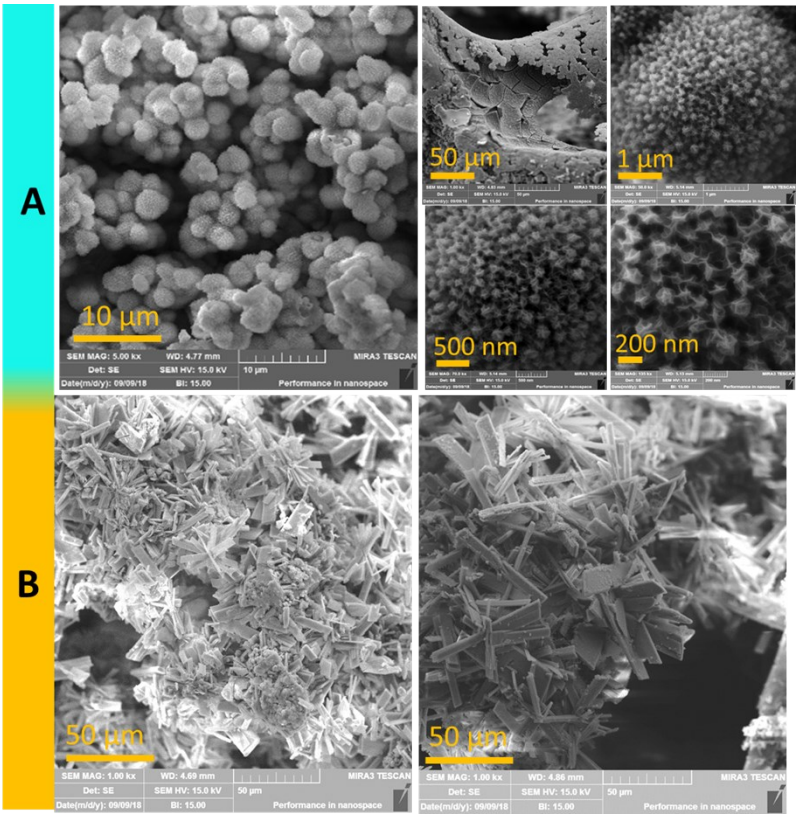

Figure S3. FE-SEM images of (A) NF/$NiCo_2O_4$ and (B) NF/$NiCo_2O_4$/MnP.

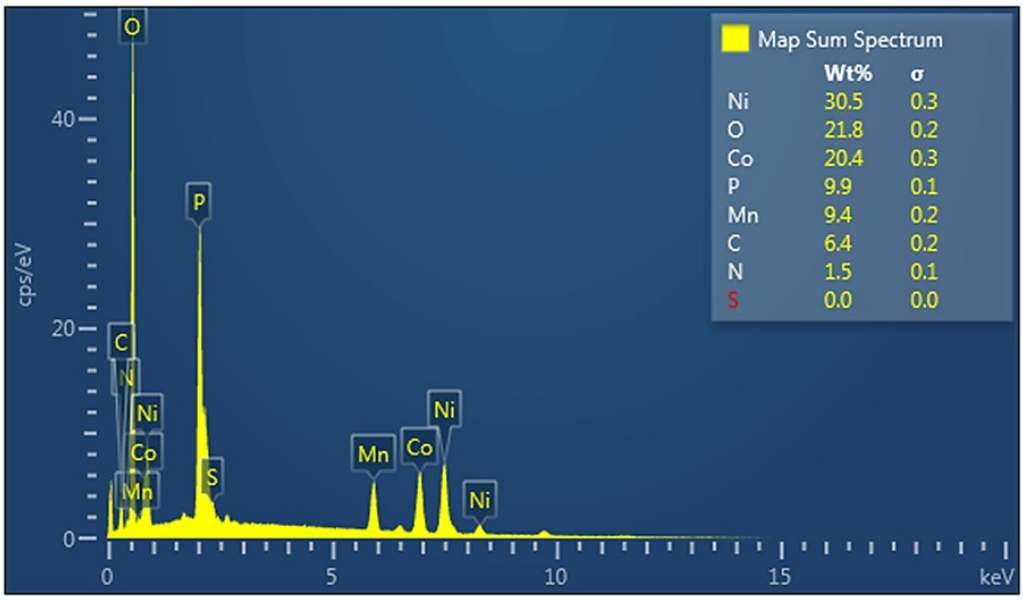

Figure S4. EDX spectrum for NF/$NiCo_2O_4$/MnP/p-Arg.

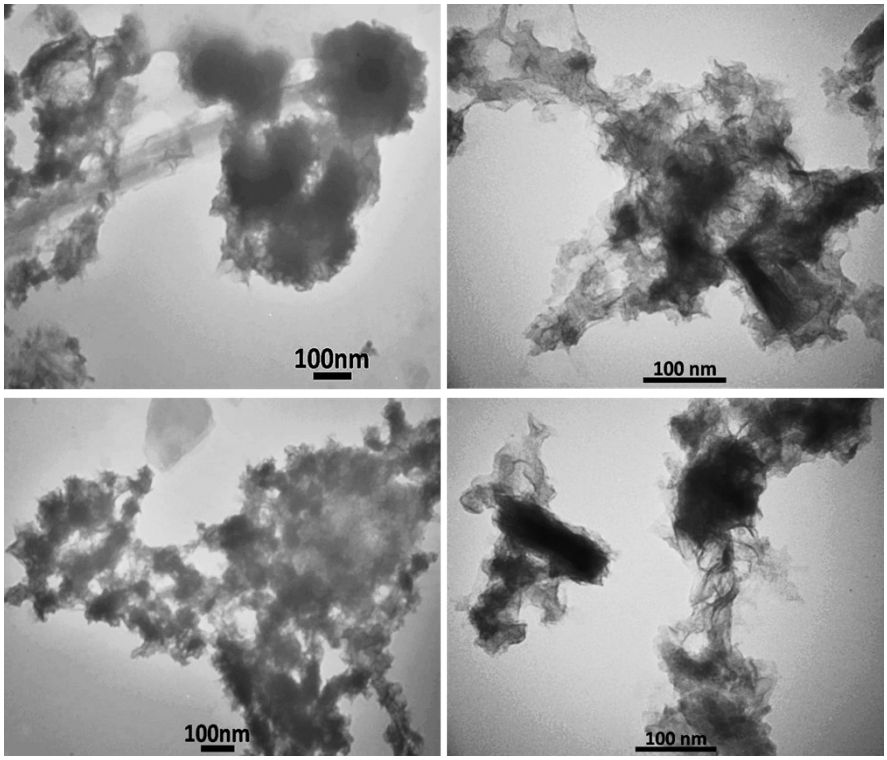

Figure S5. TEM image taken from the p-Arg film (SDS-extracted) scratched from the surface of NF.

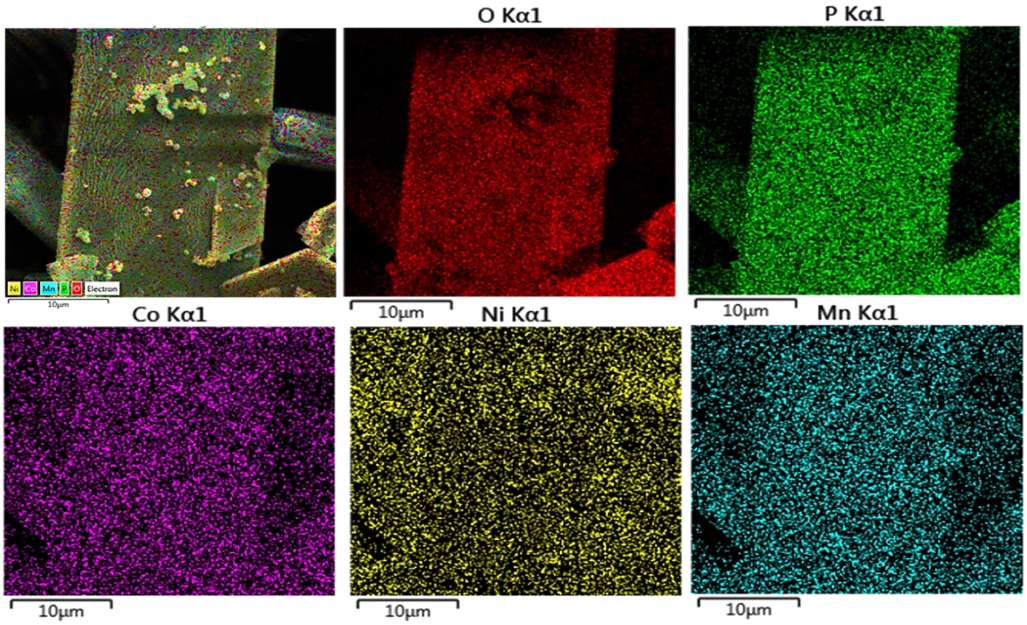

Figure S6. SEM image and corresponding EDX elemental mapping of C, O, P, Mn, Co, and Ni for NF/$NiCo_2O_4$/MnP.

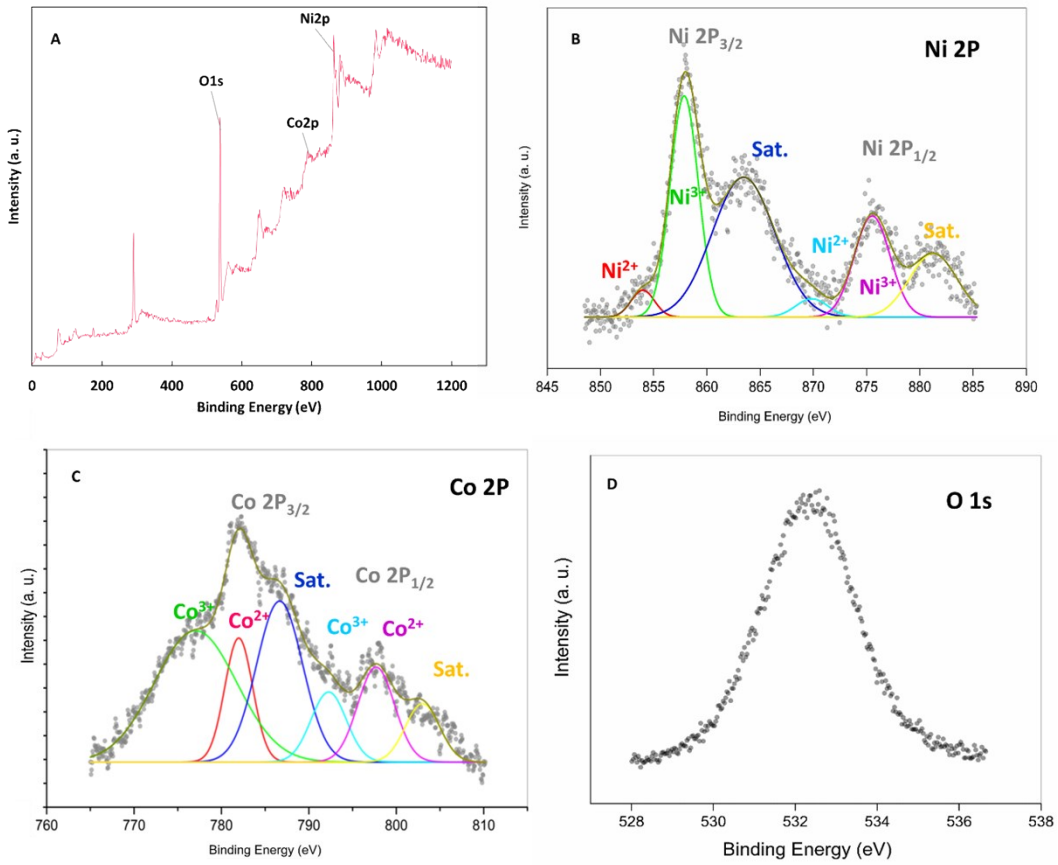

Figure S7. (A) XPS survey spectrum for NF/$NiCo_2O_4$ electrode. The magnified spectrum at (B) Ni 2p, (C) Co 2p, and (D) O 1s regions.

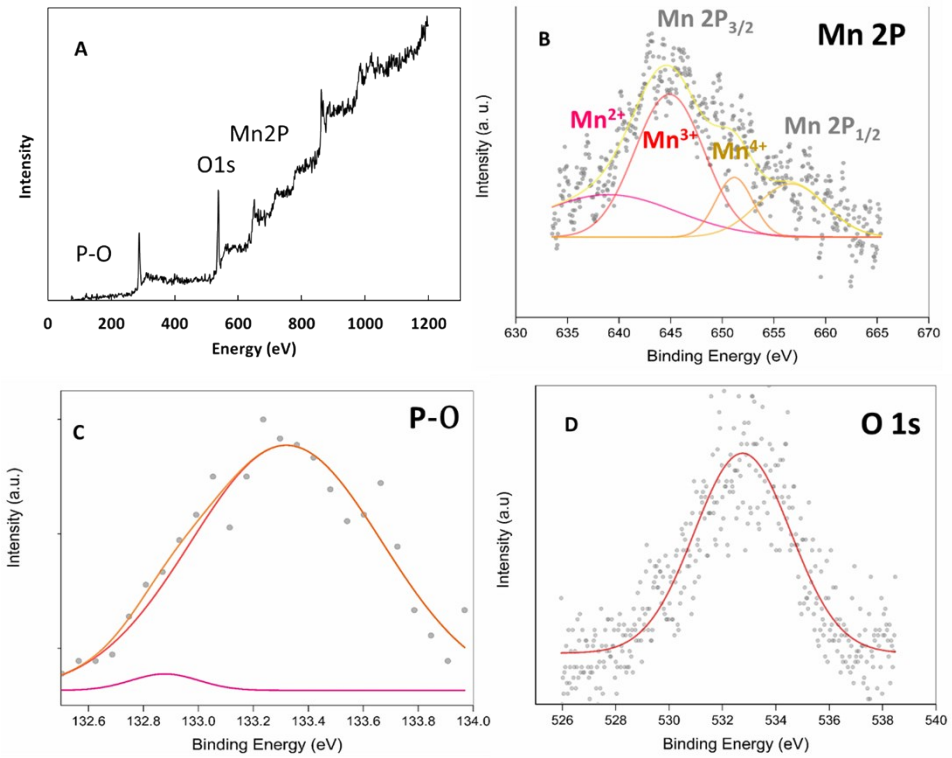

Figure S8. (A) XPS survey spectrum for NF/$NiCo_2O_4$/MnP electrode. XPS spectra in the (B) Mn 2p, (C) P-O, (D) O 1s.

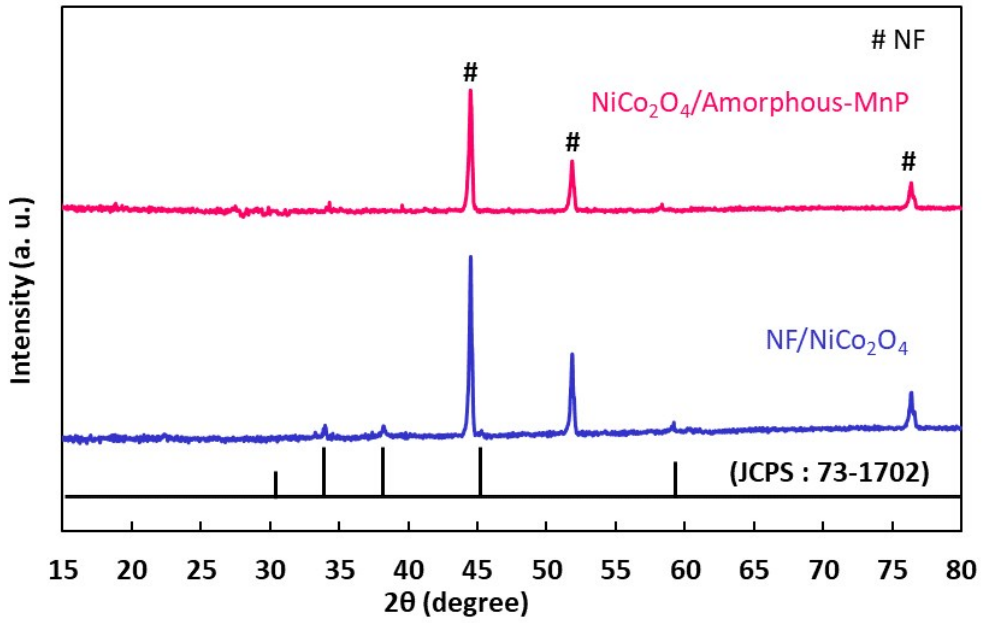

Figure S9. XRD patterns of $NF/NiCo_2O_4$ and $NF/NiCo_2O_4$/Amorphous-MnP.

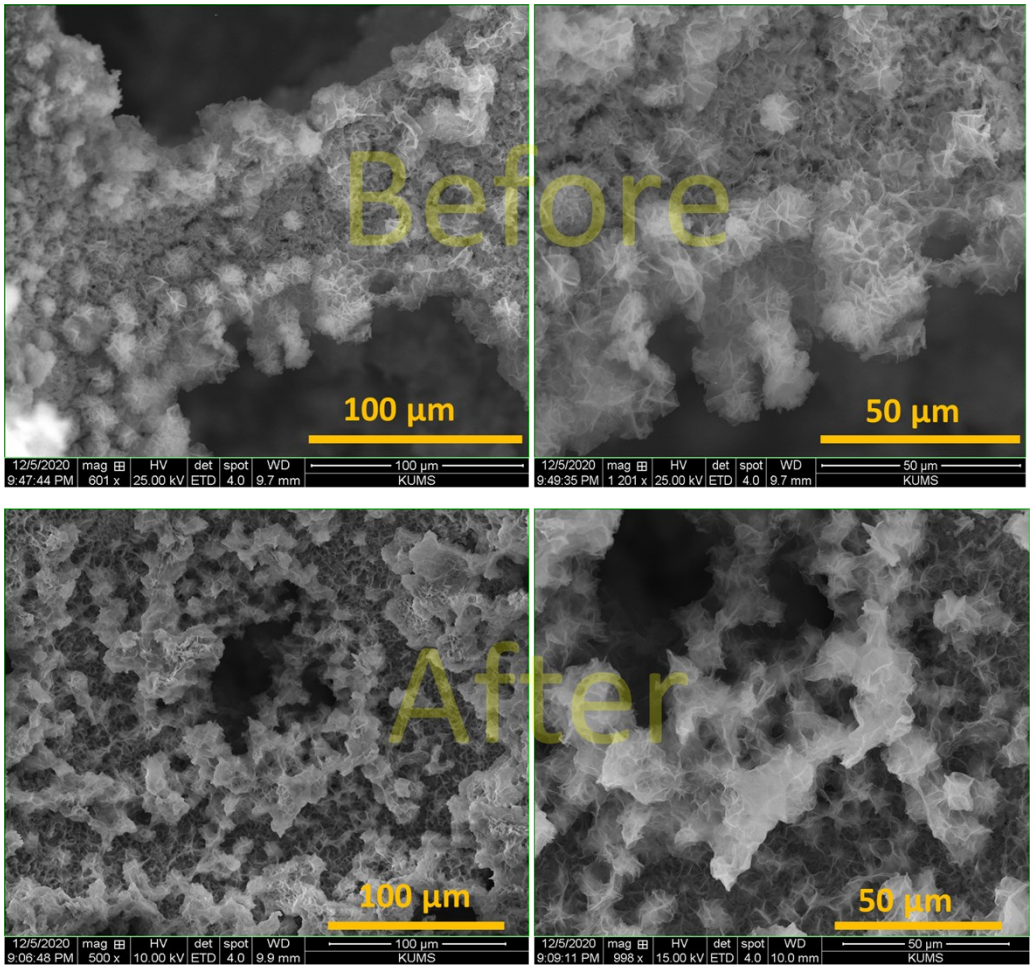

Figure S10. The SEM image taken from NF/$NiCo_2O_4$/MnP/p-Arg and beforeafter electrolysis.

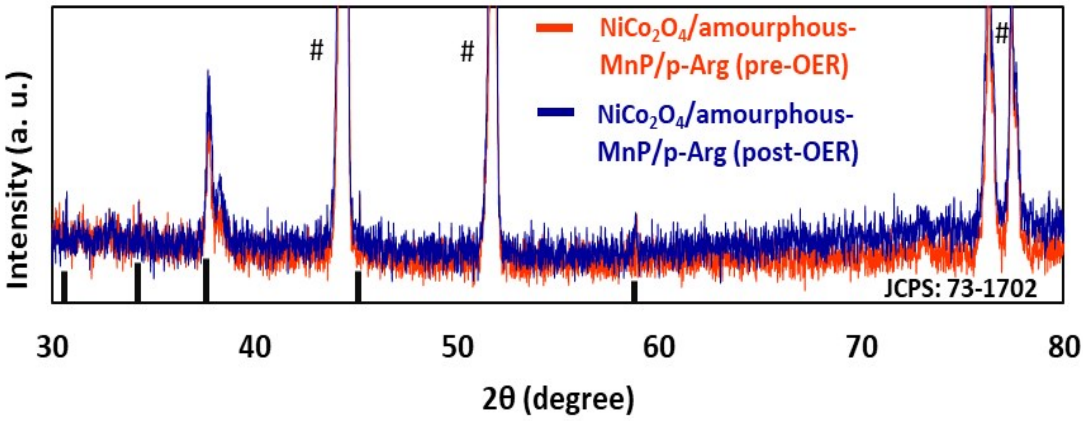

Figure S11. XRD patterns of NF/$NiCo_2O_4$/MnP/p-Arg before and after electrolysis at constant potential (# marks NF pattern).

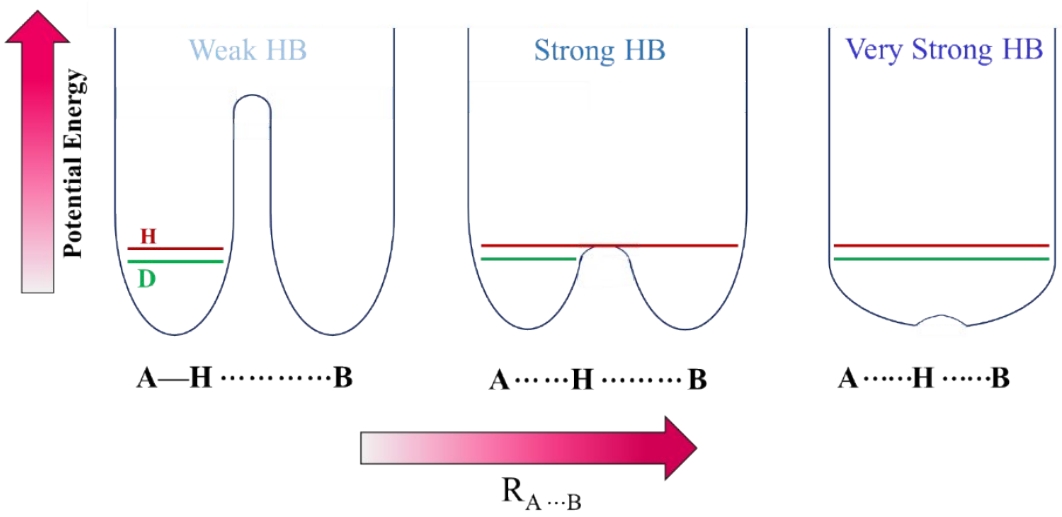

Figure S12. Schematic of zero-point energy relationships in different classes of hydrogen bonding. The potential energy wells for hydrogen-bonded heteroatoms and the zero-point energy levels for H and D are qualitatively showed for the three classes of hydrogen bonds described in Ref. S23. In very strong or single-well hydrogen bonds, right, the zero-point energies of hydrogen and deuterium both lie well above the barrier, and the hydron is shared almost equally between the heteroatoms. In proton inventory data this feature is confirmed by low fractionation factor around 0.23.

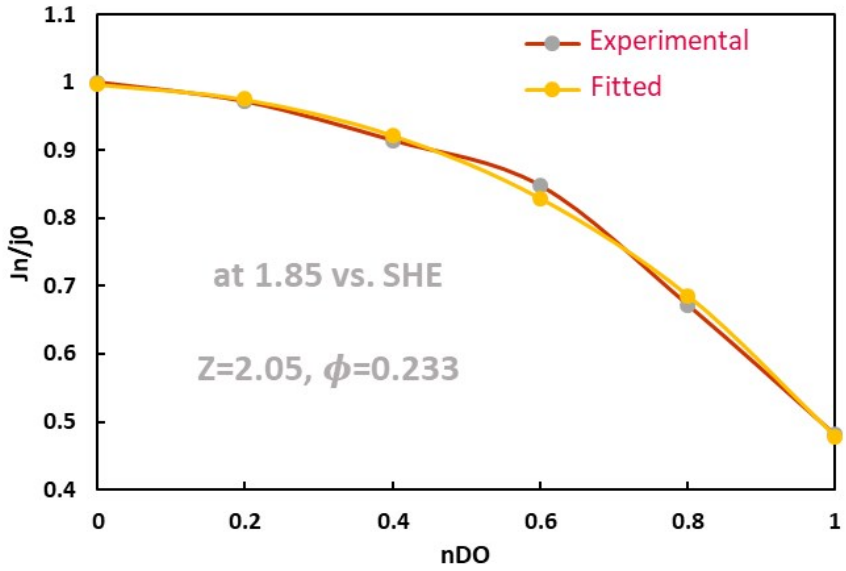

Figure S13. The plots of j_n/j_0 as a function of n, where n = [D]/([D]+ [H]) at potential 1.85 vs. SHE. Insets are the corresponding Z and $\emptyset$ values extracted from the fitted plot.

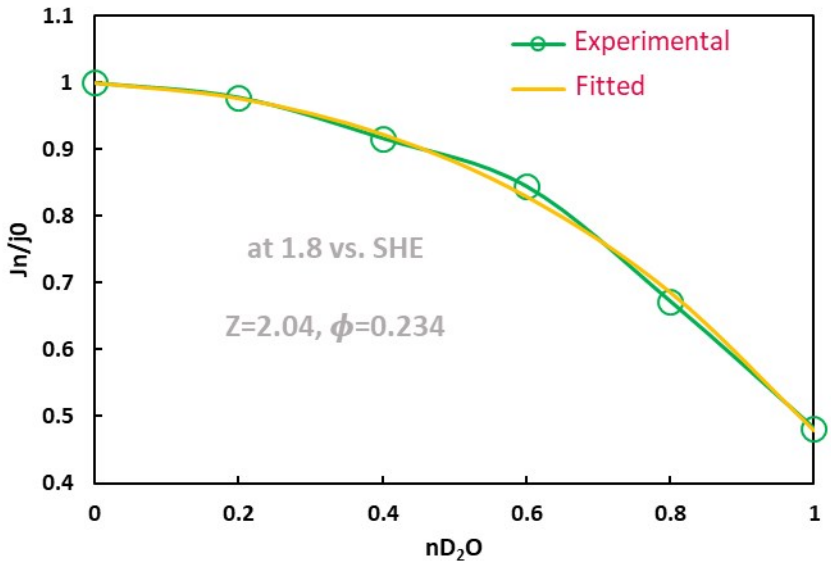

Figure S14. The plots of j_n/j_0 as a function of n, where n = [D]/([D]+ [H]) at potential 1.8 vs. SHE. Insets are the corresponding Z and $\emptyset$ values extracted from the fitted plot.

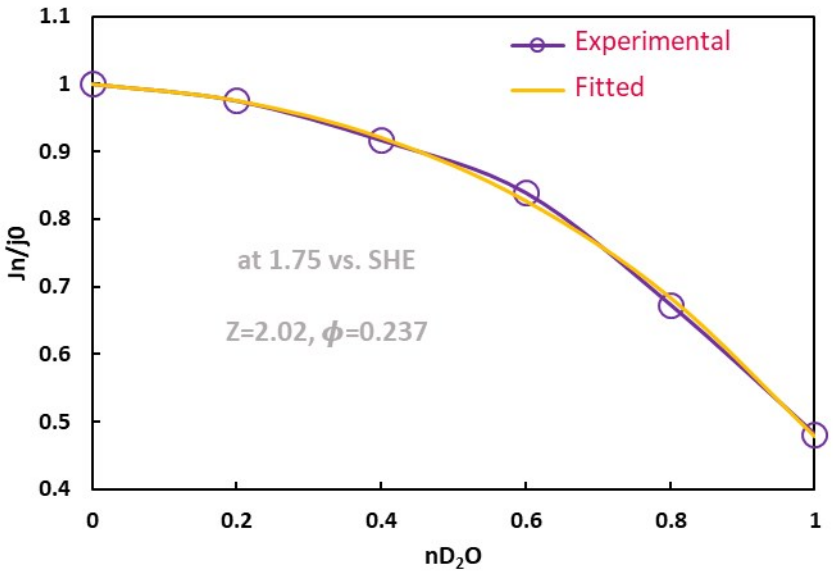

Figure S15. The plots of j_n/j_0 as a function of n, where n = [D]/([D]+ [H]) at potential 1.75 vs. values extracted from the fitted plot. ØSHE. Insets are the corresponding Z and

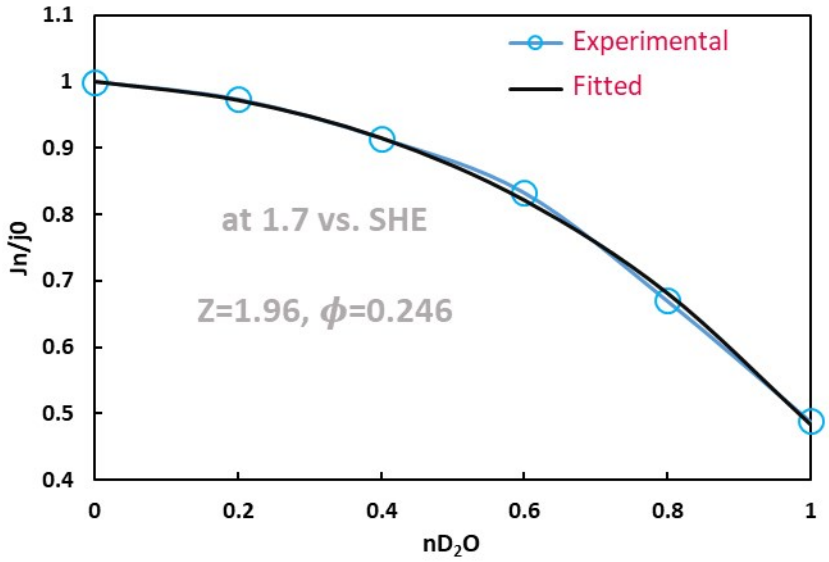

Figure S16. The plots of j_n/j_0 as a function of n, where n = [D]/([D]+ [H]) at potential 1.7 vs. SHE. Insets are the corresponding Z and $\emptyset$ values extracted from the fitted plot.

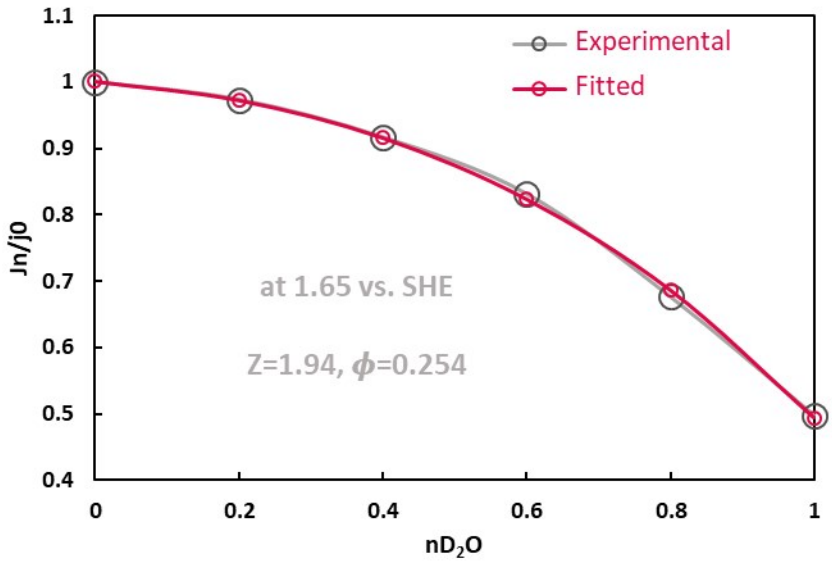

Figure S17. The plots of j_n/j_0 as a function of n, where n = [D]/([D]+ [H]) at potential 1.65 vs. SHE. Insets are the corresponding Z and ∅ values extracted from the fitted plot.

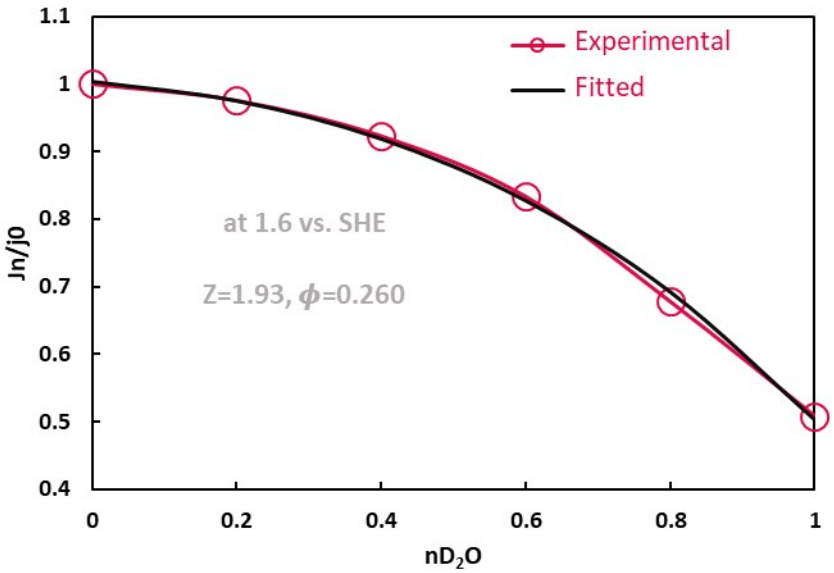

Figure S18. The plots of jn/j0 as a function of n, where n = [D]/([D]+ [H]) at potential 1.6 vs. SHE. Insets are the corresponding Z and ∅ values extracted from the fitted plot.

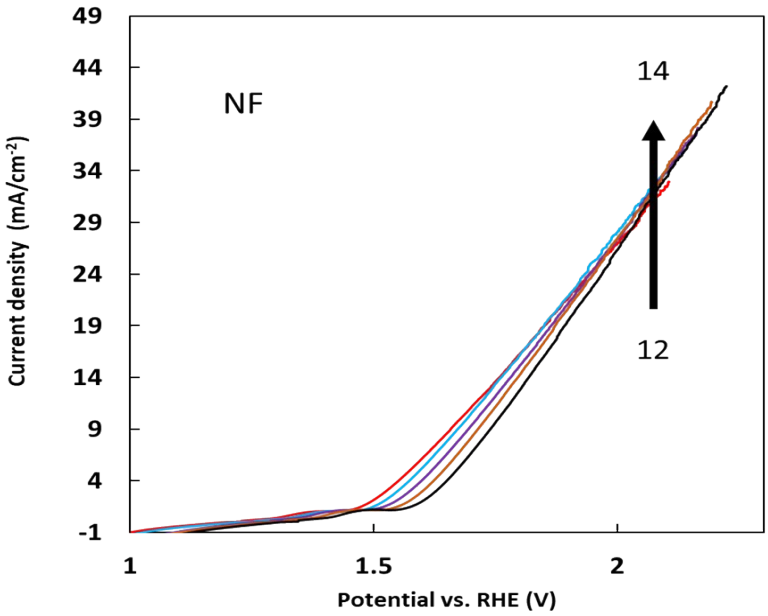

Figure S19. pH-dependent OER activity on RHE scale at NF electrode in scan rate of 5 mV s^{-1}. LSV curves were taken in KOH solutions as a function of pH.

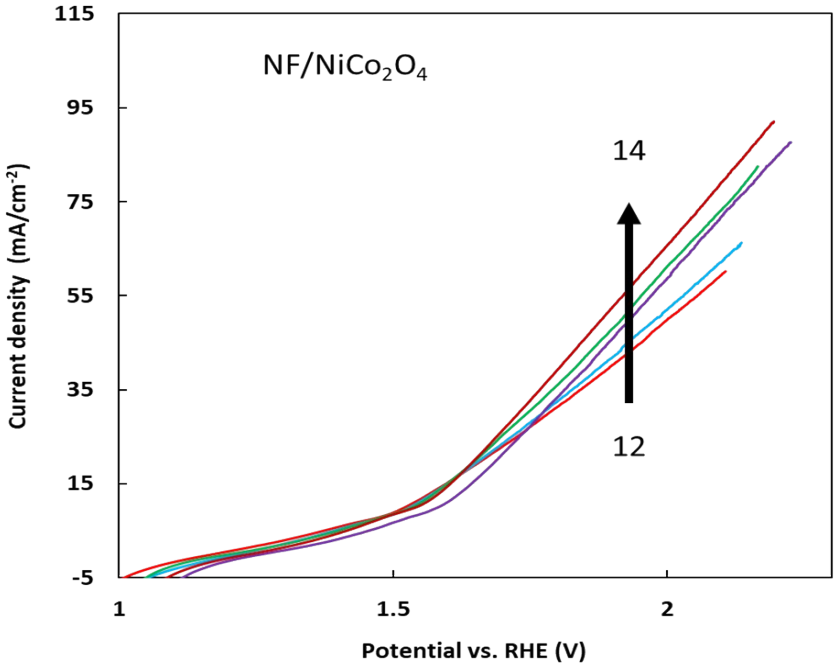

Figure S20. pH-dependent OER activity on RHE scale at $NF/NiCo_2O_4$ electrode in scan rate of 5 mV s^{-1}. LSV curves were taken in KOH solutions as a function of pH.

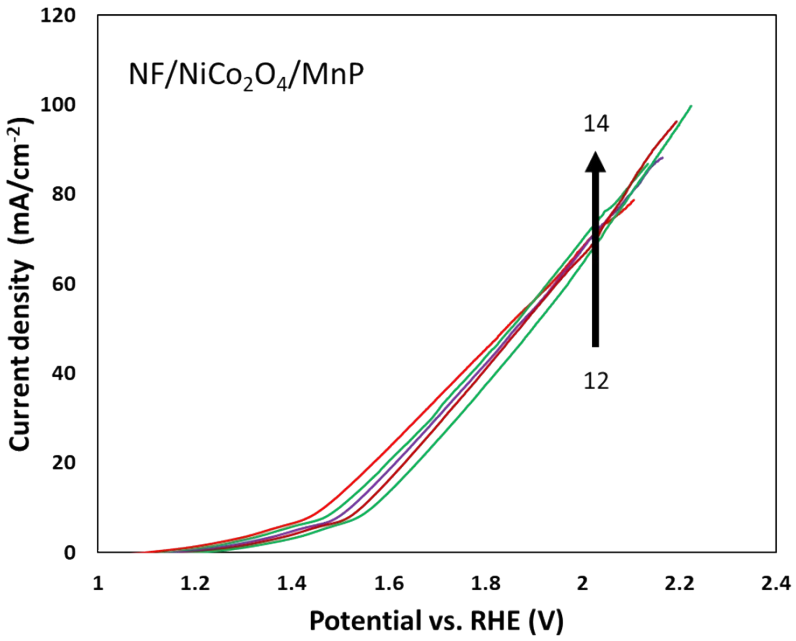

Figure S21. pH-dependent OER activity on RHE scale at NF/$NiCo_2O_4$/MnP electrode in scan rate of 5 mV s^{-1}. LSV curves were taken in KOH solutions as a function of pH.

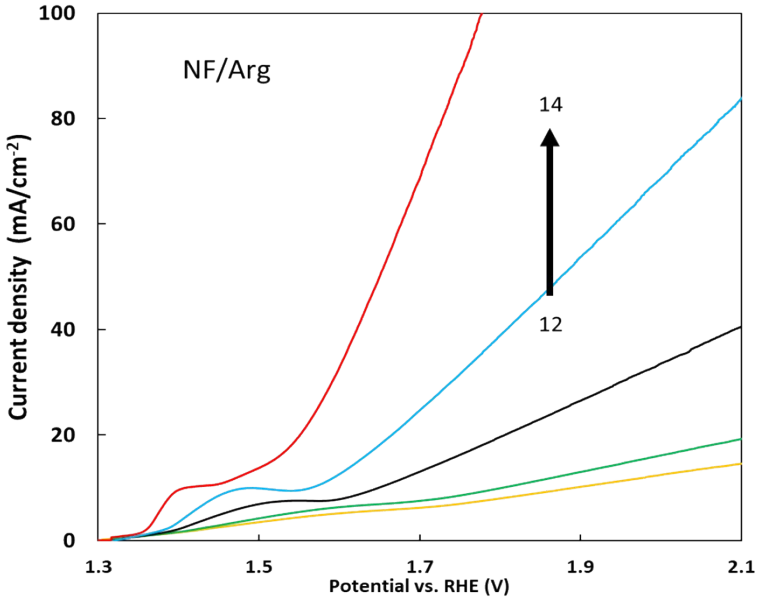

Figure S22. pH-dependent OER activity on RHE scale at NF/p-Arg electrode in scan rate of 5 mV s^{-1}. LSV curves were taken in KOH solutions as a function of pH.

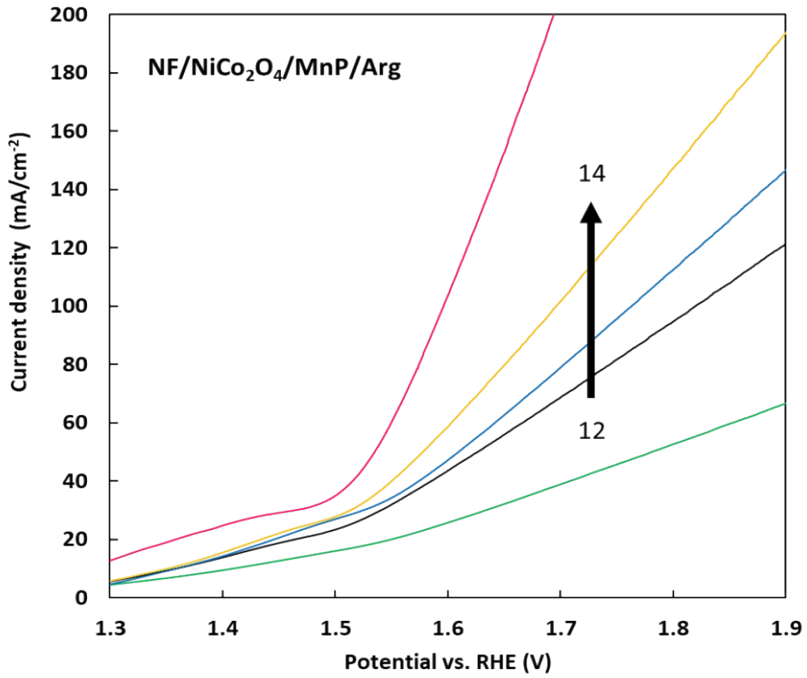

Figure S23. pH-dependent OER activity on RHE scale at NF/$NiCo_2O_4$/MnP/p-Arg electrode in scan rate of 5 mV s^{-1}. LSV curves were taken in KOH solutions as a function of pH.

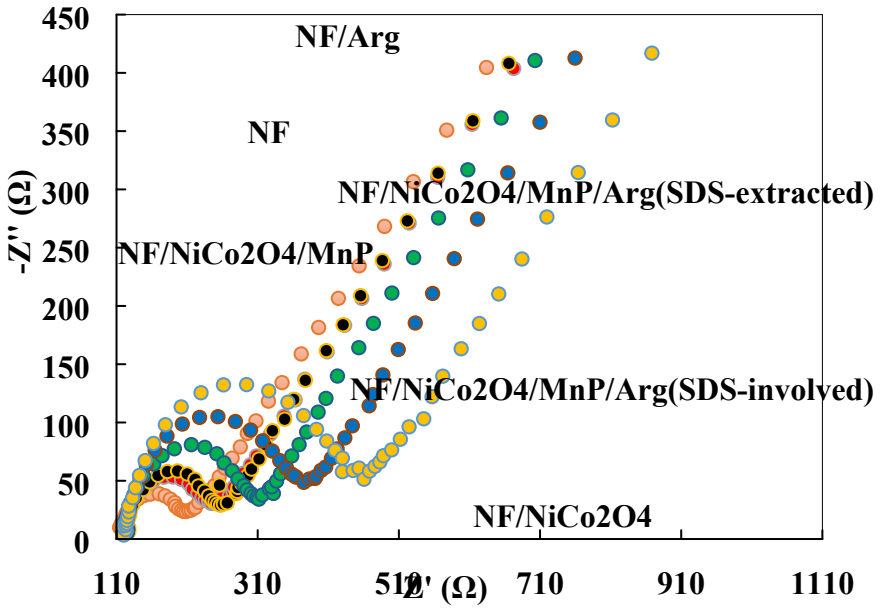

Figure S24. Electrochemical impedance spectra (EIS) of different electrodes recorded in 0.1 M KCl containing 10 mM of $Fe(CN)_6^{3-/4-}$ under open circuit potential.

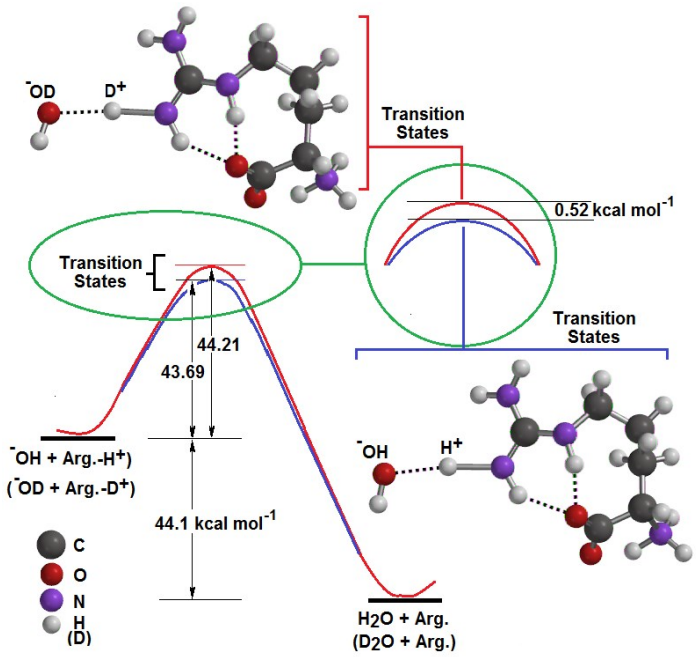

Figure S25. The diagram of energy for the proton transfer (H^+ and/or D^+) between Guanidine part of Arginine and H_2O and/or D_2O. There is not meaningful difference between the transition states energy levels ($\Delta G^{\#}$ in kcal mol^{-1}).

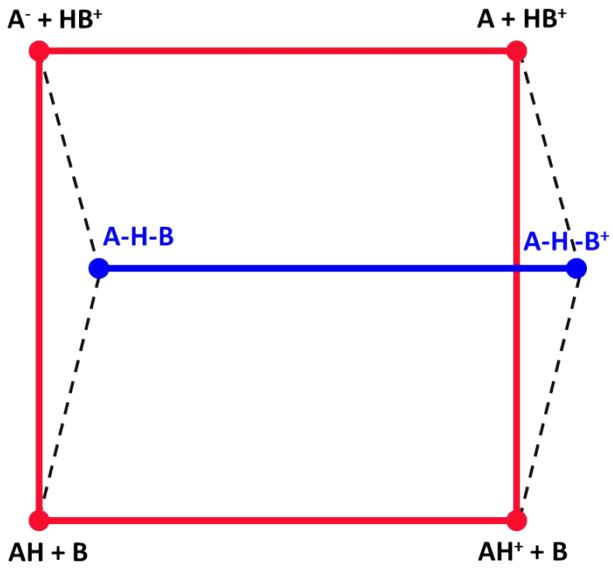

Figure S26. Schematic of the overall intermediate based on a H-bond complex intermediate proposed during a PCET for the typical half-reaction: AH + B → A + HB+e^-.

Table S1. The actual ratio of element Ni, Co and Mn at $NiCo_2O_4$/MnP by ICP-OES analysis.

Ni (mg L^{-1})	**Co (mg L^{-1})**	**Mn (mg L^{-1})**	**Percentage composition (Ni:Co)**
24350	12041	14182	66.9% : 33.1%

Table S2. Comparison of the required overpotential at J=10 mA cm^{-2} at the as prepared electrodes and recently published OER-catalysts.

Catalyste	***$\eta_{@10}$ mA cm^{-2} (mV)***	***Year***	***Solution***	***Reference***
MOF(BMM-11)	362	2019	KOH 1 M	[19]
Co-Fe-Bi/$NiCo_2O_4$	277	2020	KOH 1 M	[20]
FeP-NS/NF	220	2020	KOH 1 M	[21]
Nanoflakescatalyst (CM-NF)	377	2020	KOH 0.1 M	[22]
Ni/Cr doped Fe_3O_4	262	2020	KOH 1 M	[23]
$Ni_xCo_{(1-x)}$ $(OH)_y$	348	2020	NaOH 1 M	[24]
Co-CNPs/FTO_{250}	240	2020	KOH 0.1 M	[25]
$Co_5(PO_4)_2(OH)_4$	254	2019	KOH 1 M	[26]
$CoVO_{x-20}$	308	2019	KOH 0.5 M	[27]
Co-OOH	290	2019	KOH 1 M	[28]
NiS/NF	320	2017	KOH 1 M	[29]
Ni:FeOOH/NGF	214	2019	KOH 1 M	[30]
Ni_5P_4-Ni_2P	180	2018	KOH 1 M	[31]
Ni_3S_2 nanosheets/NF	223	2019	KOH 1 M	[32]
Fe:Ni(oHFeCe:$Ni(OH)_2$/NF	201	2018	KOH 1 M	[33]
FeCoYOx/NF	214	2019	KOH 1 M	[34]
This work (NF/$NiCo_2O_4$/MnP/GPR)	103	-	KOH 0.5 M	-
This work (NF/GPR)	183	-	KOH 0.5 M	-

Experimental

Materials and apparatus

All chemicals were analytical grade and used without further purification. Arginine (Merck, 95%), sodium dodecyl sulfate (SDS, Sigma-Aldrich, 95%) were reagent-grade materials. Other materials are; cobalt nitrate hexahydrate (Co $(NO_3)_2$. $6H_2O$, Sigma Aldrich 98%), nickel nitrate hexahydrate ($Ni(NO_3)_2$. $6H_2O$, Sigma-Aldrich, 98%), sodium phosphate monobasic dehydrate (NaH_2PO_4, Sigma Aldrich, 98%), urea (CH_4N_2O, Sigma-Aldrich, 98%), manganese (II) chloride tetrahydrate ($MnCl_2.4H_2O$, Sigma-Aldrich, 98%), potassium phosphate tribasic (K_3PO_4, Sigma Aldrich, 99%), hydrochloric acid (HCl, Merck, 37%), KOH (Sigma-Aldrich, 90%), ethanol (C_2H_5OH, Merck, 99%),acetone (C_3H_6O, Merck). Deuterated electrolytes were prepared using D_2O (Sigma-Aldrich, 99.9 atom % D, see Figure S1). All solutions were prepared with deionized water. Raman spectroscopy was done using ISB Jobin-Yvon Spex HR-320 equipped with a 600 g/mm monochromator (grating) and an SDL laser with pump wavelength of 785 nm and 140 mw output. The morphology of the samples was studied by TESCAN Mira 3 XMU field emission scanning electron microscope (Czech) coupled with energy dispersive spectroscopy (EDS).

Electrochemical measurements

Electrochemical measurements were carried out in an aqueous KOH (0.1, 0.5 and 1.0 M) where Ni foam was directly used as the working electrode without any polymer binder or conductive additive, a platinum rod as the counter electrode, and a silver/silver-chloride electrode (Ag/AgCl) as the reference electrode. All the measured potentials were converted to RHE, $E_{RHE} = E_{Ag/Agcl} + 0.059\ pH + 0.198$ V. To evaluate the OER activities of the as-peapred catalyst, the steady state voltammograms were recorded at a scan rate of 1 mV s^{-1}. Chronopotentiometry measurements were performed under the same experimental setup without IR correction. Electrochemical impedance spectroscopy (EIS) was performed by applying an alternating current voltage with 5 mV amplitude in frequency ranges of 0.01 Hz−100 kHz. The surface composition of the composite electrodes was investigated using X-ray photoelectron spectroscopy (XPS) on an ESCALAB 250Xi-Thermo Scientific. ATR-FTIR analysis was performed by DXR Microscope (Thermo Fisher™), Fourier transform infrared spectra (FT-IR) was measured by a Bruker spectrometer (Germany).

Synthesis of NF/$NiCo_2O_4$

The Ni foam (3cm × 4cm) was carefully cleaned in 3 M HCl solution in an ultrasound bath for 15 min in order to remove the surface oxide layer. Then, it was immersed in acetone to remove organic materials from the surface. Finally, it was washed thoroughly with acetone, deionized water and ethanol for 10 minutes respectively. 1 mmol of cobalt nitrate hexahydrate ($Co(NO_3)_2.6H_2O$, 0.5 mmol nickel nitrate hexahydrate ($Ni(NO_3)_2.6H_2O$, 2 mmol ammonium fluoride (NH_4F) and 3 mmol urea were dissolved in 30 ml deionized water and stirred for 15 minutes to form pink homogenous solution. Subsequently, the above solution and the treated Ni foam were transferred into 50 ml Teflon-lined stainless-steel autoclave and heated at 120 ℃ for 6 h. After being cooled to room temperature gradually, the Ni foam with a dark-green color was carefully washed with deionized water and ethanol several times and then dried at 60 ℃ for 12 h.

Synthesis of NF/$NiCo_2O_4$ /amorphous-MnP

Amorphous-MnP were decorated on $NiCo_2O_4$ cauliflower-like morphology by a hydrothermal technique. For the synthesis of the NF/$NiCo_2O_4$/amorphous-MnP electrode, 2 mmol manganese (II) chloride tetrahydrate ($MnCl_2.4H_2O$) and 0.5 g sodium phosphate monobasic dehydrate (NaH_2PO_4) were dissolved into 40 ml of water with magnetically stirred for several minutes to obtain a homogeneous solution. Then the NF/$NiCo_2O_4$ piece was immersed into the solution and transferred to a 50 mL autoclave to conduct the second hydrothermal step. The autoclave was maintained at 150 ^oC for 6 h to develop the growth of MnP microplates.

Electropolymerization of L-arginine

A piece of the substrate (bare or modified NF, 0.5 cm × 0.5 cm) was subjected for the electropolymerization of arginine through consecutive cyclic voltammetry (CV). Figure S2A shows the continuous CVs in 0.1 M phosphate buffer solution (PBS) containing 2.5 mM of arginine at pH 7.5. The electropolymerization was done over the the potential range of -1.1 to 2.3 V vs. Ag/AgCl at the scan rate of 100 mV/s for 20 cycles[1]. In a similar procedure, the electropolymerization was repeated in the presence of 8 mM of SDS, then, the prepared film was soaked in the stirred solution, 15 min, of water/ethanol mixture (1:1) to extract the trapped SDS molecule and arginine monomers, as was approved by Uv-vis spectrometry. The effect of number of cycles during electropolymerization of Arg is shown in Figure S2B. The optimum cycle number was obtained as 30.

FESEM, EDXA, TEM and ICP

All characterization studies, field emission scanning electron microscopy (FESEM) and corresponding mapping analysis, energy dispersive x-ray analysis (EDXA), x-ray photoelectron spectroscopy (XPS), and x-ray diffraction (XRD) are provided in following. Figure S3-A demonstrates the FESEM images taken from $NiCo_2O_4$ electrothermally prepared on the surface of the NF skeleton with a cauliflower-like morphology. Higher magnification identified the array of wrinkled polyhedral structures with an average diameter of 160±25 nm. Figure S3B displays the electrochemically synthesized MnP microplates, which densely embedded in the substrate. The mapping analyses indicate Ni, Co, O, Mn, P are homogenously deposited on the surface of $NF/NiCo_2O_4/MnP$ electrode (Figure S6). The morphological features of sample were investigated with a Zeiss (EM10C-Germany) transmission electron microscope (TEM) operating at 100 kV. These images were prepared as follows: After scratching the prepared p-Arg film on NF, the dilute aqueous solution of the sample was sonicated for 15 min. Then, a portion of sample (20 μL) was dropped onto formvar carbon film on copper grid 300 mesh (EMS-USA) and dried thoroughly at room temperature. The inductively coupled plasma optical emission spectrometer (ICP-OES) was tested by Perkin Elmer Optima 2000DV.

XPS studies

The compositions and electronic states of the as-prepared sub-layers, $NF/NiCo_2O_4$ and $NF/NiCo_2O_4/MnP$, were studied by X-ray photoelectron spectroscopy (XPS). The overall spectra in Figures S7A and S8A illustrate the surveys of the XPS spectrum for both interfaces $NF/NiCo_2O_4$ and $NF/NiCo_2O_4/MnP$ respectively. Figure S7A displays a high-resolution spectrum comprised of two major peaks at 857.8 and 875.6, corresponding to Ni 2p3/2 and Ni 2p1/2, which showed a spin-orbit energy difference of 17.8, confirming the formation of $NiCo_2O_4$[2] . The results of the Gaussian fitting indicated two spin-orbit singlets related to Ni^{3+} and two shakeup satellites. The XPS spectra shown in Figure S7C is respective to cobalt with four peaks, two spin-orbit doublets at 782.2 and 798.1 eV, with the spin-orbit splitting of 15.9 eV, characteristic of Co 2p3/2 and Co 2p1/2 and two satellites. The resolved peaks indicate the coexistence of Co^{3+}/Co^{2+} in the prepared sample [3, 4]**.** Additionally, two shakeup satellites were identified at 787.1 and 804.6 eV due to a charge-transfer satellite structure. The spectrum at the region of O1s specifies a metal-coordinated bond located at 538.2 (Figure S7D), meanwhile no further shoulder was detected related to other contributions of oxygen in OH and physicochemical water adsorbed species[5]. Three kinds of chemical states including Mn^{2+}, Mn^{3+} and Mn^{4+} were identified at the Mn $2P_{3/2}$ region. Two main peaks were detected at 644.6 and

656.9 eV (Figure S8B). In Figure S8C, we considered the P 2p region with a single peak at 133.1 eV, related to the P—O bond, as was expected. It was accompanied by O 1s detected at 532.6 eV (Figure S8D).

XRD analysis

Figure S9 displays the results of X-ray diffraction (XRD). indicating diffraction peaks at 2θ values of 33.9°, 38.8°, 45.5° and 59.3° that can be indexed as the (111), (220), (311) and (440) crystal planes of $NiCo_2O_4$ (JCPDS NO.73- 1702)[6-8] . The thre strong peak peaks of the Ni substrate are marked by "#". The results displays no distinct peak other than that from the apparent $NiCo_2O_4$/NF substrate, suggesting the formed MnP film is amorphous[9, 10].

Computational studies

In this study, some of the appropriate molecular mechanics (MM) and quantum mechanical (QM) methods were applied for the optimization of the discussed polymer structure. The interpretation of the results is based on the best results of the optimization and minimization of the structures. The molecular mechanics (MMFF94) and DFT-B3LYP were run by the *Spartan'16* package. A further insight was gained through a profile of the arginine polymer with the proton channel modeled by the MM method (MMFF94) (Figure 7E-G). The length of the polymer cluster was calculated 53.36 Å and the diameter of the channel was obtained 15.82 Å. Further calculation (DFT-B3LYP/6-31G*) was performed to investigate the isotope effect, where the diagram of the proton-transfer $H^+(D^+)$ energy between the guanidine part of arginine and H_2O/D_2O (Figure S25). There is not a meaningful difference between the transition-state energy-levels ($\Delta G^{\#}$ in kcal mol^{-1}). The obtained ΔG (kcal mol^{-1}) of both processes (H^+/D^+ proton transfer) was 44.10 kcal mol^{-1}. The obtained $\Delta G^{\#}$ (kcal mol^{-1}) of both processes were 43.69 (H^+) and 44.21(D^+) kcal mol^{-1}, respectively. The minor difference between the free activation energies and the transition states ($\Delta\Delta G^{\#}$) was about 0.5 kcal mol^{-1}. The calculated rate constants for the H^+ and/or D^+ proton transfer was calculated as $1.637\text{x}10^{-13}$ and $1.636\text{x}10^{-13}$, respectively, indicating a minor difference in kinetics of $H^+(D^+)$. The absolute ratio of the rate constants (k_H/k_D) was obtained as 1.001. The results of experiments showed relatively higher values (1.3-1.5), which can be due to the simplification of the overall process during modeling, and possible perturbation in the PCET mechanism caused by multiple experimental parameters e.g. the effect of solution base.

Supporting Notes:

Supporting Note 1. Kinetic Isotope Effects

KIEs were studied via electrochemical methods. The LSVs were recorded with a scan rate of 5 mV s^{-1} the experiments were carried out in pH adjusted aqueous KOH solution and K_3PO_4 in D_2O solution, the corresponding current densities at a certain overpotential of η were abbreviated as J(H_2O) and J(D_2O). The current density can be expressed by J=nFkC*, where n = total number of electrons transferred, k = heterogeneous rate constant, and C^* = bulk concentration [11]. Dividing J in proteo solution to J in dutero solution gives:

$$\frac{J_{H_2O}}{J_{D_2O}} = \frac{n_H k_H C_H^*}{n_D k_D C_D^*} \qquad \text{eqn. S1}$$

Since the measurements were performed in solutions with the equal pH(D), the concentration of hydroxide and deuteroxide are same, $C_H^* = C_D^*$, and by assuming unify n values in both solutions, KIE could be written as:

$$\text{KIEs}_{\text{H/D}} = \left[\frac{k_{H_2O}}{k_{D_2O}}\right]_\eta = \left[\frac{J_{H_2O}}{J_{D_2O}}\right]_\eta \qquad \text{eqn. S2}$$

When measuring pH with the glass electrode in deuterated solution, we often add a constant value of 0.41, pD=pH+0.41. This correction was done via the calculation of electrochemical potential difference between an H_2|Pt electrode in H_2O and a D_2|Pt electrode in D_2O[12]. Because no OER dependency observed on [K_3PO_4], it was used as a proton-less basic agent in D_2O solution.

Supporting Note 2. Proton inventory studies

The fitting of the experimental proton inventory data and calculations of the respective parameters (Z and ∅) were done through the Equation (1) in the main text, which was derived from the Kresge-Gross-Butler (Eqn. S3),[13]. This equation has been established to describe isotope effect arise from the combination of the isotope effect at a few sites, with the ∅ values

quite different from one, and from a *Z*-effect, an aggregate isotope effect originated from most of sites with ∅ values individually close to unity [14]:

$$K_n = K_0 \left[\frac{\prod_{i=1}^{x} (1 - n + n\phi Ti)}{\prod_{i=1}^{x} (1 - n + n\phi Ri)} \right] Z^n \qquad \text{eqn. S3}$$

where k_0 is the kinetic rate constant in deutero solution, k_n is the kinetic rate constant in proteo solution. n is the mole fraction of D_2O, x is the number of hydrogenic sites in the reactant/transition state, $\emptyset_{Ti}$ and $\emptyset_{Ri}$ are the isotopic fractionation factor for hydrogenic site in the transition- and reactant-state, respectively. Zn describe the Z-effect, for Z = 1, there are no Z-sites contribution in the isotope effect; for Z > 1, the Z-sites deliver an inverse isotope effect, and for Z < 1, the Z-sites contribute a normal isotope effect[15-17]If we assume a single hydrogenic site, the eqn. S3 could be simplified as :

$$K_n = K_0 \left[\frac{(1 - n + n\phi T)}{(1 - n + n\phi R)} \right] Z^n \qquad \text{eqn. S4}$$

We assumed the pronounced kinetics isotope effect occurs at a single hydrogenic site, thus, the x was equal to 1. Assuming J≈k, a simplified form of eqn. S4 is:

$$\frac{j_n}{j_0} = (1 - n + n\phi_{Ti})Z^n \qquad \text{eqn. S5}$$

Equation S5 was used to fit the proton inventory data, which showed a non-linear dome-shaped curve observed in the case of combination of normal and inverse contributions. A linear curve conveys a single site, a quadratic curve two sites, a cubic curve three sites, and finally an exponential curve indicate an infinite-site model. [13, 14, 18]. There are two types of fractionation factors conveyed for hydrogen-transfer reactions on small molecules that involve a *transition-state hydrogen bridge*. These two-category pass through a transition-state hydrogen bridges; (I) When the transfer of proton happens through RDS, the labeled hydrogen has an important effect in the reaction-coordinate motion, herein, KIE about 2 to 10 are expected. (II) Another case is when PT is accompanied with another reaction, ET and/or heavy-atom reorganization (such a

bond formation between heavier elements than hydrogen). The minimum value of KIE and fractionation factor are 1.5 and 0.3, respectively[15, 17].

Supporting Note 3. pH-dependency on RHE scale and atom proton transfer studies

The LSV for pH studies were recorded with a scan rate of 5 mV s^{-1} at different pH values adjusted by KOH solution. All potentials of the measured data were converted into the RHE scale. To convert the standard hydrogen electrode (SHE) scale to the RHE scale, we used the relation εRHE = εSHE +59 mV×pH.[19-34]

The reaction order of the concentration for OH^- is expressed by eqn. S6, where *j* is the current density (mA) at a certain overpotential of η, $[OH^-]$ is the concentration of hydroxide in electrolytes (mol L^{-1}).

$$\rho_{[OH^-]} = \left[\frac{\partial \log J}{\partial \log [OH^-]}\right]_{\eta} \qquad \text{eqn. 11}$$

Based on the dissociation equilibrium of water, pH+pOH=14, the reaction order of $[OH^-]$can be described as function of pH, as is in eqn. S7:

$$\rho_{[OH^-]} = \left[\frac{\partial \log J}{\partial \log [-14+pH]}\right]_{\eta} = \left[\frac{\partial \log J}{\partial\, pH}\right]_{\eta} \qquad \text{eqn. S7}$$

In order to designate the involvement of PT in RDS of the catalytic reaction, the dependence of OER activity on an additional Lewis base, PO_4^{-3}, The reaction order of PO_4^{-3} ($\rho[PO_4^{-3}]$) was estimated according to eqn. S8:

$$\rho_{[PO_4^{-3}]} = \left[\frac{\partial \log j}{\partial \log [PO_4^{-3}]}\right]_{\eta} \qquad \text{eqn. S8}$$

Supporting references

1. J. Soleymani, M. Hasanzadeh, M. Eskandani, M. Khoubnasabjafari, N. Shadjou and A. Jouyban, *Materials science and engineering: C*, 2017, **77**, 790-802.
2. Y. Gong, Z. Yang, Y. Lin, J. Wang, H. Pan and Z. Xu, *Journal of Materials Chemistry A*, 2018, **6**, 16950-16958.
3. K. Akbar, J. H. Jeon, M. Kim, J. Jeong, Y. Yi and S.-H. Chun, *ACS Sustainable Chemistry & Engineering*, 2018, **6**, 7735-7742.
4. S. M. N. Jeghan and G. Lee, *Nanotechnology*, 2020, **31**, 295405.
5. Y. Lin, Z. Yang, D. Cao and Y. Gong, *CrystEngComm*, 2020, **22**, 1425-1435.
6. S. Liu, L. Hu, X. Xu, A. A. Al-Ghamdi and X. Fang, *Small*, 2015, **11**, 4267-4283.
7. C. Pan, Z. Liu, W. Li, Y. Zhuang, Q. Wang and S. Chen, *The Journal of Physical Chemistry C*, 2019, **123**, 25549-25558.
8. H. Shi and G. Zhao, *The Journal of Physical Chemistry C*, 2014, **118**, 25939-25946.
9. Y. Li and C. Zhao, *Chemistry of Materials*, 2016, **28**, 5659-5666.
10. R. D. Smith, M. S. Prévot, R. D. Fagan, Z. Zhang, P. A. Sedach, M. K. J. Siu, S. Trudel and C. P. Berlinguette, *Science*, 2013, **340**, 60-63.
11. A. J. Bard and L. R. Faulkner, *Electrochemical Methods*, 2001, **2**, 580-632.
12. K. A. Rubinson, *Analytical Methods*, 2017, **9**, 2744-2750.
13. A. Kohen and H.-H. Limbach, *Isotope effects in chemistry and biology*, cRc Press, 2005.
14. P. F. Fitzpatrick, *Biochimica et Biophysica Acta (BBA)-Proteins and Proteomics*, 2015, **1854**, 1746-1755.
15. Y. Liu and C. C. McCrory, *Nature communications*, 2019, **10**, 1-10.
16. R. L. Schowen, *Journal of Labelled Compounds and Radiopharmaceuticals: The Official Journal of the International Isotope Society*, 2007, **50**, 1052-1062.
17. K. Venkatasubban and R. L. Schowen, *Critical Reviews in Biochemistry*, 1984, **17**, 1-44.
18. S. Haschke, M. Mader, S. Schlicht, A. M. Roberts, A. M. Angeles-Boza, J. A. Barth and J. Bachmann, *Nature communications*, 2018, **9**, 1-8.
19. L. Zhong, J. Ding, X. Wang, L. Chai, T.-T. Li, K. Su, Y. Hu, J. Qian and S. Huang, *Inorganic Chemistry*, 2020, **59**, 2701-2710.
20. U. P. Suryawanshi, M. P. Suryawanshi, U. V. Ghorpade, M. He, D. Lee, S. W. Shin and J. H. Kim, *ACS Applied Energy Materials*, 2020, **3**, 4338-4347.
21. F. Yang, X. Chen, Z. Li, D. Wang, L. Liu and J. Ye, *ACS Applied Energy Materials*, 2020, **3**, 3577-3585.

22. S. Bera, W.-J. Lee, E.-K. Koh, C.-M. Kim, S. Ghosh, Y. Yang and S.-H. Kwon, *The Journal of Physical Chemistry C*, 2020.
23. M. Cai, W. Liu, X. Luo, C. Chen, R. Pan, H. Zhang and M. Zhong, *ACS Applied Materials & Interfaces*, 2020, **12**, 13971-13981.
24. H. R. Devi, R. Nandan and K. K. Nanda, *ACS Applied Materials & Interfaces*, 2020, **12**, 13888-13895.
25. N.-U.-A. Babar and K. S. Joya, *ACS omega*, 2020.
26. X. Bu, C. Chiang, R. Wei, Z. Li, Y. Meng, C. Peng, Y. Lin, Y. Li, Y. Lin and K. S. Chan, *ACS applied materials & interfaces*, 2019, **11**, 38633-38640.
27. M. A. Ehsan, A. S. Hakeem, M. Sharif and A. Rehman, *ACS omega*, 2019, **4**, 12671-12679.
28. S. Hao, G. Zheng, S. Gao, L. Qiu, N. Xu, Y. He, L. Lei and X. Zhang, *ACS Sustainable Chemistry & Engineering*, 2019, **7**, 14361-14367.
29. J.-T. Ren and Z.-Y. Yuan, *ACS Sustainable Chemistry & Engineering*, 2017, **5**, 7203-7210.
30. M. P. Suryawanshi, U. V. Ghorpade, S. W. Shin, U. P. Suryawanshi, E. Jo and J. H. Kim, *ACS Catalysis*, 2019, **9**, 5025-5034.
31. J. Xu, J. P. Sousa, N. E. Mordvinova, J. D. Costa, D. Y. Petrovykh, K. Kovnir, O. I. Lebedev and Y. V. Kolen'ko, *Acs Catalysis*, 2018, **8**, 2595-2600.
32. M. Yao, B. Sun, L. He, N. Wang, W. Hu and S. Komarneni, *ACS Sustainable Chemistry & Engineering*, 2019, **7**, 5430-5439.
33. Q. Zhang, S. Zhang, Y. Tian and S. Zhan, *ACS Sustainable Chemistry & Engineering*, 2018, **6**, 15411-15418.
34. Q. Zhang, N. Liu and J. Guan, *ACS Applied Energy Materials*, 2019, **2**, 8903-8911.